Journal of
Synchrotron
Radiation

ISSN 0909-0495

Received 17 February 2012
Accepted 29 July 2012

Single-exposure dual-energy-subtraction X-ray imaging using a synchrotron source

R. P. Carnibella,[a,b]* A. Fouras[a,b] and M. J. Kitchen[c]

[a]Division of Biological Engineering, Monash University, Wellington Road, Clayton, Victoria 3800, Australia, [b]Department of Mechanical and Aerospace Engineering, Monash University, Wellington Road, Clayton, Victoria 3800, Australia, and [c]School of Physics, Monash University, Wellington Road, Clayton, Victoria 3800, Australia. E-mail: richard.carnibella@monash.edu

Projection radiography of the chest has long been plagued by the presence of bony anatomy obscuring visibility of the lungs and heart. Dual-energy subtraction is a well known method for differentiating bone and soft tissue, but existing techniques are not ideally suited to dynamic imaging. Herein a new technique to address this problem is presented. The harmonic content of a monochromated X-ray beam is exploited, and two in-line detectors are used to perform single-exposure dual-energy imaging. Images of a phantom demonstrate the ability to both separate and quantitatively measure the thickness of constituent materials, whilst images of a mouse thorax demonstrate the ability to separate bone and soft tissue in a biological specimen. The technique is expected to improve the performance of dynamic lung imaging.

Keywords: dual-energy imaging; digital subtraction imaging; basis material decomposition; dynamic imaging; X-ray imaging.

1. Introduction

Two significant problems with projection X-ray imaging are the difficulty in differentiating superimposed structures and the related problem of quantitatively measuring the material properties of individual structures. Dual-energy X-ray imaging is one technique which can overcome these limitations. Consequently, some of the applications of dual-energy imaging include bone differentiation on chest X-rays for the purpose of improving tumour diagnosis (Fraser *et al.*, 1986; Kelcz *et al.*, 1994), the diagnosis of cerebral haemorrhage (Brockmann *et al.*, 2010), lung perfusion measurement (Thieme *et al.*, 2008), cardiac imaging (Schwarz *et al.*, 2008), the diagnosis of urinary calculi (Graser *et al.*, 2008) and gout (Choi *et al.*, 2009), and bone and fat density measurement (Sartoris & Resnick, 1989; Jensen *et al.*, 1995).

Growing interest in dynamic synchrotron X-ray imaging has created demand for new methods of performing dual-energy imaging, which can be used with a synchrotron source and which are suitable for dynamic imaging. In particular, there is need for a means of subtracting bone from dynamic lung images. The shadows produced by the ribcage and spine are a problem for regional lung volume measurement techniques (Kitchen *et al.*, 2008), which regard the chest as a two-component system consisting of air and soft tissue. Regional lung volume measurements, from dynamic image sequences recorded at synchrotrons, have enabled researchers to assess the efficacy of ventilation strategies employed to safely aerate the lungs of premature neonates born with poor lung function (Hooper *et al.*, 2009). In other studies, researchers have quantified the mechanics of lung tissue associated with detecting early-stage pulmonary disease using synchrotron-based imaging techniques (Fouras *et al.*, 2012). In that work the visibility of the ribcage was artificially suppressed in order to isolate the motion of the lung tissue.

An alternative to dual-energy imaging for bone subtraction has been developed by Suzuki *et al.* (2006), using a massive training artificial neural network. That approach, however, can be impractical because of the number of training samples required. A recent study (Kitchen *et al.*, 2011) showed that dynamic lung image segmentation can be performed in the context of phase-contrast X-ray imaging, using a Laue analyser crystal, to reconstruct the complex refractive index of a two-material system. However, that technique is complicated by the ultra-small-angle scattering arising from the airways, which increases the complexity of the reconstruction procedure.

Digital dual-energy imaging was pioneered by Brody *et al.* (1981) and Lehmann *et al.* (1981) who outlined the theory of basis material decomposition and demonstrated bone and soft tissue subtraction on chest X-ray images. They used a rapidly switching polychromatic X-ray source to sequentially capture low- and high-energy images (dual exposures). In this set-up the delay between capturing the dual-energy images limits the rate at which dynamic imaging can be performed and means rapidly moving subjects are prone to motion artefacts. Xu *et al.* (2011) developed a dual-energy system using flat panel detectors with a 15 ms delay, which can acquire image pairs at

up to 15 frames a second. Another issue, pertaining to the use of a polychromatic source, is the non-linear relationship between the log intensity measurements and material thickness (Brody *et al.*, 1981). The problem is not intractable, but requires extensive calibration and is often handled qualitatively by adjusting a weighting factor until satisfactory material subtraction is achieved.

An alternative to dual-exposure approaches is to selectively capture X-rays of different energies from a single exposure to polychromatic radiation, rather than changing the source energy. Single-exposure dual-energy imaging systems (Speller *et al.*, 1983; Ishigaki *et al.*, 1986) have been developed, which consist of a piece of metal, acting as a high-pass X-ray filter, sandwiched between two imaging plates or film-screen cassettes. By simultaneously capturing low- and high-energy images, motion artefacts are eliminated. Such an analogue detection medium is not, however, suitable for dynamic imaging. Phillips are developing a dual-layer sandwich detector (Phillips, 2008), which will be able to simultaneously record dual-energy images, but to date the technology is not commercially available.

To perform dual-energy tomography with a synchrotron source, Torikoshi *et al.* (2001, 2003) designed a system using the harmonic energy content of a monochromated X-ray beam to provide dual energies and used a rotating filter to alternatingly image at each energy.

The method presented in this paper is an evolution of the early single-exposure systems, optimized to work with a synchrotron source and digital detectors. Like Torikoshi *et al.* (2001, 2003), a key feature of the technique is the use of the harmonic energy content of a monochromated X-ray beam, but here we simultaneously acquire images at both energies using two detectors. The harmonic beam allows better energy separation than polychromatic sources and also significantly simplifies the systems of equations that need to be solved. Consequently, more accurate results can be expected, with the method only requiring a relatively simple calibration procedure. The paper first outlines the system design and theory of material decomposition. We then present experimental results from a phantom to demonstrate the accuracy of the technique followed by images of a mouse thorax to demonstrate the ability to separate bone from the soft tissues.

2. Theory and method

2.1. X-ray harmonics for dual-energy imaging

Silicon crystals are commonly used to produce a monochromatic beam from a polychromatic X-ray source. In accordance with Bragg's law,

$$n\lambda = 2d\sin\theta, \tag{1}$$

where n is an integer, λ is the wavelength of the incident wave, d is the distance between scattering planes and θ is the angle between the incident wave and scattering planes, photon energy can be selected by adjusting the angle θ at which the X-ray beam strikes the crystal. Different orders n result in the presence of harmonic frequencies in the reflected beam at the same angle. Usually these harmonics are unwanted and efforts are taken to suppress them. For example, with double-crystal monochromators the first crystal is commonly detuned.

The experiments undertaken here were performed in experimental hutch 3 of beamline 20B2 at the SPring-8 synchrotron in Japan (Goto *et al.*, 2001). A Si(111) double-crystal monochromator was used to produce a beam with a fundamental energy of 17 keV and a third harmonic of 51 keV [the second harmonic for the Si(111) reflection is forbidden]. Although higher-order harmonics (*e.g.* the fifth, seventh, *etc.*) exist, their contribution can be neglected because each harmonic becomes progressively weaker.

Ideally, a higher fundamental energy than 17 keV is desirable for imaging macroscopic objects. However, this energy was chosen because the Gd_2O_2S:Tb (P43) phosphors used in the detectors have a *K*-edge at 50.2 keV. By placing the third-harmonic energy just beyond this (51 keV), the efficiency of the phosphor is maximized.

2.2. Dual detectors

The imaging set-up used in these experiments is illustrated in Fig. 1. A key feature is that the two phosphor screens are positioned in-line with the beam. A mirror (1 mm-thick aluminium-coated soda lime glass) angled at 45°, also on the same axis, was used to transfer the image on the first screen to a digital camera. In addition to the mirror, between the two screens was a 3 mm-thick sheet of aluminium, which acts as a high-pass energy filter.

For the front detector a PCO 4000 CCD camera (14 bit, pixel size 9.0 µm × 9.0 µm, 4000 pixels × 2672 pixels) coupled to a Nikon 105 macro lens (1.8:1 demagnification for an effective pixel size of 16.2 µm) was used in combination with a custom-made phosphor screen. The screen consisted of a

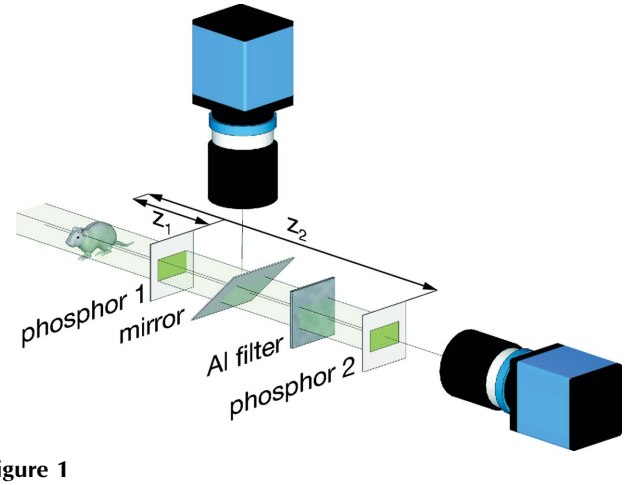

Figure 1
Single-exposure dual-energy imaging set-up using a synchrotron source. Initially the beam is dominated by the fundamental (low) energy component. An aluminium plate acts as a high-pass filter so that subsequently the harmonic (high) energy component dominates. Two phosphors and cameras simultaneously capture the low- and high-energy images. z_1 and z_2, the distances between the sample and detectors, were 8 cm and 36 cm, respectively.

1 mm-thick quartz glass substrate, powder-coated with a 25 μm layer of P43 phosphor. For the rear detector a Hamamatsu C9300-124 CCD camera (12 bit, same Kodak CCD as the PCO 4000) with fibre-optic taper (1.8:1) was employed (Uesugi *et al.*, 2011). The fibre-optic coupling provided a high numerical aperture to increase the sensitivity for the lower-intensity second image. This configuration was used for all experiments presented in this paper.

To account for differences in alignment and magnification between detectors, a pair of images was taken of an object containing three small metallic fiducial markers. Image registration was performed using these images to produce an affine transform that could correct for discrepancies in translation, scale, rotation and shear between images recorded by the two detectors.

The rationale in choosing the materials and thicknesses of the first phosphor screen, mirror and aluminium filter was to find a balance between minimizing the contribution of the fundamental energy at the second detector while preserving the higher-energy harmonic component. The goal was that the first and second cameras in this set-up are essentially operating as low- and high-energy detectors, respectively. The actual proportion of each energy at each detector is taken into account in the decomposition process.

2.3. Material decomposition

The attenuation of X-rays by any material is an energy-dependent function of photoelectric absorption and X-ray scattering. By measuring the combined attenuation of two known materials, at two different energies, it is possible to solve for the thickness of each material (Lehmann *et al.*, 1981). The following explains how this was achieved for the imaging set-up described in the previous section.

The transmittance through each material in the path of the beam, as a function of energy, can be expressed using the Beer–Lambert attenuation law as

$$k(E) = I/I_0 = \exp[-\mu(E)t], \tag{2}$$

where I_0 and I are the intensity of the incident and transmitted beam, respectively, $\mu(E)$ is the material's linear attenuation coefficient at energy E, and t is its thickness.

The phosphor's (P43) output in the visible spectrum can be expressed as a function of its quantum efficiency (QE),

$$I(E) = S(E)[1 - k_{\mathrm{P43}}(E)]\,\mathrm{QE}_{\mathrm{P43}}(E), \tag{3}$$

where $S(E)$ is the source strength.

The total transmittance measured by each detector is equivalent to the flat-field (direct beam) corrected image,

$$T_1 = \frac{k_{\mathrm{sample}}(E_1)\,I_1(E_1) + k_{\mathrm{sample}}(E_2)\,I_1(E_2)}{I_1(E_1) + I_1(E_2)} = \frac{\mathrm{image}_1}{\mathrm{image}_{1,\mathrm{flat}}}, \tag{4}$$

$$T_2 = \frac{\prod^M [k_m(E_1)]k_{\mathrm{sample}}(E_1)I_2(E_1) + \prod^M [k_m(E_2)]k_{\mathrm{sample}}(E_2)I_2(E_2)}{\prod^M [k_m(E_1)]I_2(E_2) + \prod^M [k_m(E_2)]I_2(E_2)} = \frac{\mathrm{image}_2}{\mathrm{image}_{2,\mathrm{flat}}}, \tag{5}$$

where, for the second detector, M is the number of other materials the beam passes through in addition to the sample (*i.e.* the first phosphor screen, the mirror and the aluminium filter). E_1 and E_2 are the energy of the fundamental and third harmonic, respectively.

Grouping constants, these expressions can be simplified to

$$T_1 = C_1 k_{\mathrm{sample}}(E_1) + C_2 k_{\mathrm{sample}}(E_2), \tag{6}$$

$$T_2 = C_3 k_{\mathrm{sample}}(E_1) + C_4 k_{\mathrm{sample}}(E_2), \tag{7}$$

for the first and second detectors, respectively.

The constants C_n are the fractions of the total measured transmittance attributable to each energy. If these constants are known, the sample's transmittance and then the thickness of each material can be found by solving the following simultaneous equations,

$$\begin{bmatrix} k_{\mathrm{sample}}(E_1) \\ k_{\mathrm{sample}}(E_2) \end{bmatrix} = \begin{bmatrix} C_1 & C_2 \\ C_3 & C_4 \end{bmatrix}^{-1} \begin{bmatrix} T_1 \\ T_2 \end{bmatrix}, \tag{8}$$

$$\begin{bmatrix} t_1 \\ t_2 \end{bmatrix} = \begin{bmatrix} \mu_1(E_1) & \mu_2(E_1) \\ \mu_1(E_2) & \mu_2(E_2) \end{bmatrix}^{-1} \begin{bmatrix} \ln^{-1}[k_{\mathrm{sample}}(E_1)] \\ \ln^{-1}[k_{\mathrm{sample}}(E_2)] \end{bmatrix}, \tag{9}$$

where $\mu_m(E)$ is the linear attenuation coefficient of sample material m at energy E, and t_m is its thickness. The linear attenuation coefficients used in this paper can be found in Table 1.

For decomposition of biological samples, the aim is to separate bone from soft tissue, where bone is relatively homogeneous in its composition but not its density, and soft tissue broadly includes skin, muscle, fat, internal organs, *etc.* The simplification of the body as a two-component system is valid because, in terms of attenuation, the difference between the two components can primarily be attributed to the calcium content of bone. This can be verified by observing that in the NIST database (NIST, 2011) the attenuation coefficients of various soft tissues (brain, breast, lung, muscle, ovary and testis) differ from that of water at 17 keV by at most 15% (breast). In comparison, the attenuation coefficient of bone is over 900% that of water.

2.4. Calibration

Calibration is necessary for two reasons. Firstly, because energy separation in this system is not perfect: the low-energy detector measures a small fraction of the high-energy component and *vice versa*. Secondly, calibration is a means of accounting for all the materials between the sample and second detector without specifically needing to know the attenuation coefficients of each.

Table 1
Linear attenuation coefficients (cm^{-1}) (NIST, 2011).

	17 keV	51 keV
Aluminium	14.88	0.9608
PMMA	0.9675	0.2446
Cortical bone (ICRU-44)	12.15	0.7863
Soft tissue (ICRU-44)	1.297	0.2370

The constants C_n can be determined by imaging at least two different calibration samples for which the sample's thickness and attenuation coefficients are known. For the following experiments the two calibration samples imaged were 1 mm and 2 mm sheets of aluminium. The total transmittance for each detector was calculated; for example, for the first calibration sample at the first detector,

$$T_{1,\mathrm{calib1}} = \frac{I_{1,\mathrm{calib1}} - I_{\mathrm{dark}}}{I_{\mathrm{flat}} - I_{\mathrm{dark}}}. \tag{10}$$

The theoretical transmittance, $k_n(E)$, of calibration sample n was calculated using equation (1). Table 1 gives the attenuation coefficients for aluminium at both energies used in this paper. Finally, the following simultaneous equations can be solved to obtain the calibration constants,

$$\begin{bmatrix} C_1 \\ C_2 \end{bmatrix} = \begin{bmatrix} k_1(E_1) & k_1(E_2) \\ k_2(E_1) & k_2(E_2) \end{bmatrix}^{-1} \begin{bmatrix} T_{1,\mathrm{calib1}} \\ T_{1,\mathrm{calib2}} \end{bmatrix}, \tag{11}$$

$$\begin{bmatrix} C_3 \\ C_4 \end{bmatrix} = \begin{bmatrix} k_1(E_1) & k_1(E_2) \\ k_2(E_1) & k_2(E_2) \end{bmatrix}^{-1} \begin{bmatrix} T_{2,\mathrm{calib1}} \\ T_{2,\mathrm{calib2}} \end{bmatrix}. \tag{12}$$

3. Results and discussion

3.1. Phantom image decomposition

A simple phantom, modelling the superposition of soft tissue and bone, was constructed consisting of an aluminium step wedge, with 1.5 mm-thick steps, placed in front of a plastic (PMMA) rod with a diameter of 10 mm (Fig. 2*a*).

The images captured by each detector and the results of material decomposition are also presented in Fig. 2. The results show that the two materials have been clearly separated. Furthermore, for the most part, accurate quantitative values of the material thicknesses have been obtained. The largest discrepancy evident is in the thickness of the second (3 mm) aluminium step. The explanation for this discrepancy illustrates two important issues that arose over the course of conducting these experiments.

The first issue was the choice of energies. At 17 keV less than 2% of X-rays will be transmitted through a 3 mm-thick piece of aluminium. This results in the first detector, nominally the low-energy detector, being totally dominated by the high-energy component. Theoretically, this should not be an issue because both detectors are treated as dual-energy detectors according to the theory outlined in the previous section. However, when approaching the limit in which little of the low-energy beam is transmitted through the sample, the equations become ill-conditioned and errors are magnified. A fundamental energy of around 25 keV would have been preferable, but this would place the third harmonic at 75 keV. At such a high energy the phosphor is much less sensitive and absorption contrast is diminished. A crystal monochromator capable of producing a second harmonic, which was not readily available for these experiments, could be expected to perform significantly better at energies of 25.5 and 51 keV.

The second issue was the shape and stability of the beam. The combination of the harmonic energy being physically narrower, in addition to having a narrower rocking curve than the fundamental energy, resulted in the system being sensitive to drift and intensity fluctuations of the harmonic component. When operating on images taken at different time points, *e.g.* flat-field images and calibration images, even a small shift of the harmonic can result in the introduction of significant errors. We estimate the error arising in the calculation of the transmittance at the second detector alone to be as much as 4% per pixel of vertical displacement of the harmonic. During

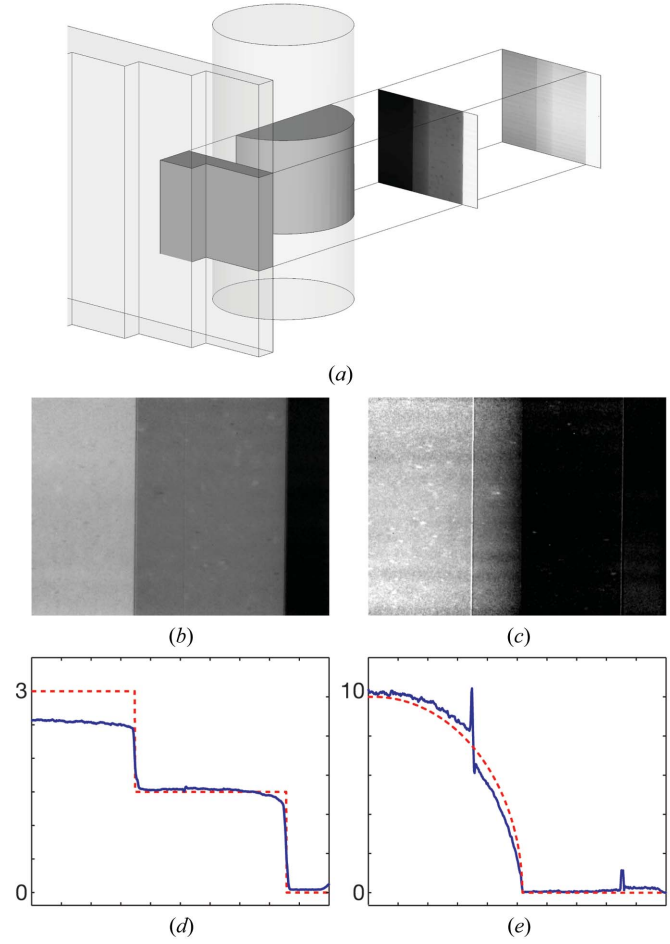

Figure 2
(*a*) Region of plastic rod and aluminium step wedge imaged using the dual-energy set-up. (*b*) Thickness of the aluminium wedge extracted by dual-energy decomposition. (*c*) Thickness of the plastic rod. The solid blue lines in (*d*) and (*e*) are the averaged cross-sectional thickness (mm) through each material; the dotted red lines are the actual thickness. The horizontal scale in subfigures (*b*)–(*e*) is consistent; ticks on the horizontal axes in (*d*) and (*e*) are spaced 1 mm apart.

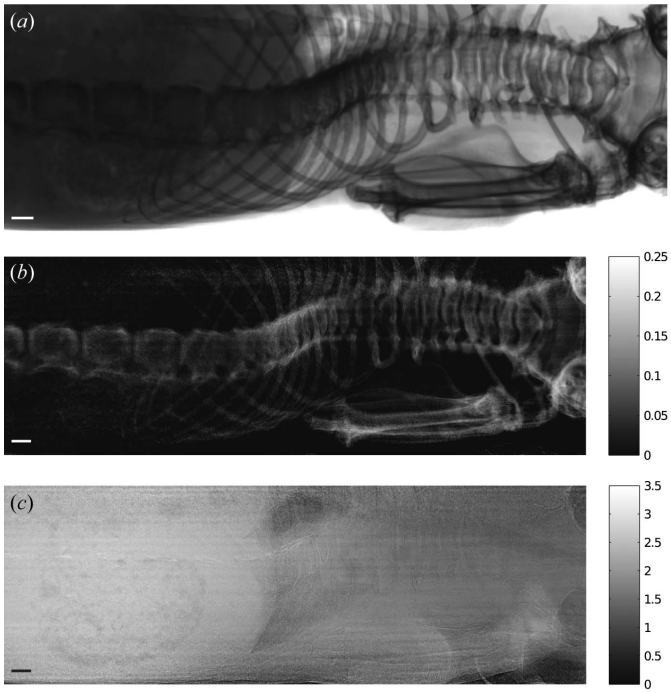

Figure 3
(*a*) Plain X-ray image recorded by the first (low-energy) detector. (*b*) Bone image obtained by dual-energy subtraction. (*c*) Soft tissue image. In addition to separating these components the thickness (in cm) of each material is given. Bars in the lower left corner of each subfigure are 1 mm long.

the course of the experiments we estimate the rate of vertical harmonic drift at around 1.3 pixels min^{-1}. To compensate for the effects of this drift, the harmonic peaks were manually realigned before performing operations on images taken at different time points. The results in Figs. 2 and 3, in comparison with those obtained without this compensation (not shown), show a significant improvement in accuracy. Ideally, a more stable beam or more thorough beam tracking throughout the experiment could have further improved the quality of the results.

As a final observation, the image of the rod thickness (Fig. 2*c*) shows the presence of strong vertical lines corresponding to the edges of the aluminium step. These are the result of propagation-based phase contrast (Snigirev *et al.*, 1995; Wilkins *et al.*, 1996) produced by the edges of the step wedge. The decomposition algorithm outlined in this paper is based on a model of absorption contrast and therefore does not account for the effects of diffraction. The simplest measure to reduce phase contrast is to minimize the distance between the sample and detectors, since this phase contrast is propagation-based. It should also be pointed out that in biological samples such abrupt sharp edges are rare so that at short propagation distances phase contrast is much weaker.

3.2. Mouse thorax image decomposition

A small mouse was also imaged and a decomposition performed to separate bone from soft tissue. The results are presented in Fig. 3. Qualitatively, we see that the bones have been clearly separated from the soft tissue. In Fig. 3(*c*) the shadow or impression of the bones that have been removed is visible upon close inspection. In some situations this is not desirable, for example with correlation-based lung motion tracking algorithms (Fouras *et al.*, 2011), in which case adding the equivalent bone thickness back to the soft tissue thickness will remove, or at least significantly reduce, these shadows.

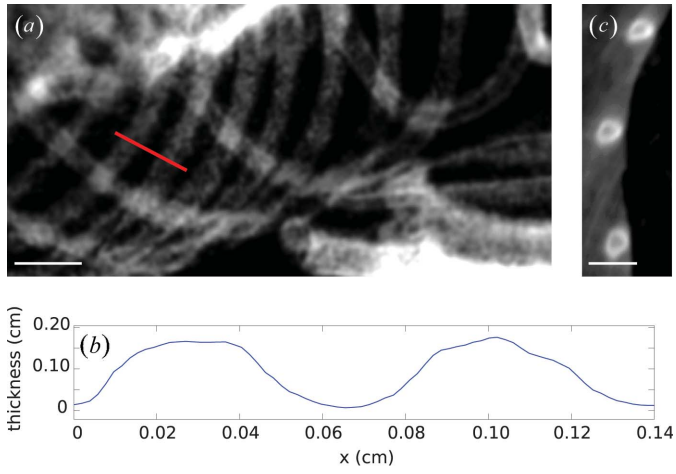

Figure 4
(*a*) Bone image (projected thickness) of a section of a mouse ribcage. An averaged cross section through the two ribs cut by the diagonal red line can be seen in (*b*). (*c*) A CT cross section through some ribs from a similar mouse, highlighting their non-uniform bone density. Bars in the lower left corner of subfigures (*a*) and (*c*) are 1 mm long.

Quantitative values for both the thickness of bone and soft tissue are in keeping with the external dimensions of the mouse. In Fig. 4(*a*), which is a magnified bone image of a section of the ribcage, a cross section through two ribs measures their thickness to be approximately half their width (Fig. 4*b*). A computed-tomography (CT) cross section through some mouse ribs is also presented (Fig. 4*c*), which highlights their non-uniform bone density. The discrepancy in thicknesses can be understood by considering that dual-energy decomposition is specifically measuring the thickness of cortical (compact) bone, and, because most bones are less dense in the centre (cancellous or spongy), this technique will tend to underestimate their anatomical thickness.

A final point is that these were static images of a deceased mouse. In theory the only limitation to the speed of dynamic imaging with this method is the intensity of the beam and sensitivity of the detectors, since low- and high-energy images are taken simultaneously. With a bright synchrotron source and high-sensitivity digital detectors, we anticipate that quantitative image reconstruction will be possible at video frame rates. This remains the work of future studies.

4. Conclusion

A single-exposure method for performing dual-energy-subtraction imaging with a synchrotron source has been presented. The accuracy of the technique for performing qualitative measurement of material thicknesses and the ability to separate bone and soft tissue in a small animal

specimen have been demonstrated. This method has applications for improving the performance of dynamic lung imaging techniques performed with synchrotron sources.

The authors gratefully acknowledge support from Australian Research Council (ARC) grants (Grant Nos. DP110101941 and DP110101498). RPC is a recipient of an Australian Postgraduate Award. MJK is an ARC Australian Research Fellow. We acknowledge useful discussions with R. A. Lewis in the preparation of this paper. We acknowledge travel funding provided by the International Synchrotron Access Program (ISAP) managed by the Australian Synchrotron.

References

Brockmann, C., Scharf, J., Nölte, I. S., Seiz, M., Groden, C. & Brockmann, M. A. (2010). *Clin. Neuroradiol.* **20**, 231–235.
Brody, W. R., Butt, G., Hall, A. & Macovski, A. (1981). *Med. Phys.* **8**, 353–357.
Choi, H. K., Al-Arfaj, A. M., Eftekhari, A., Munk, P. L., Shojania, K., Reid, G. & Nicolaou, S. (2009). *Ann. Rheum. Dis.* **68**, 1609–1612.
Fouras, A., Allison, B. J., Kitchen, M. J., Dubsky, S., Nguyen, J., Hourigan, K., Siu, K. K. W., Lewis, R. A., Wallace, M. J. & Hooper, S. B. (2012). *Ann. Biomed. Eng.* **40**, 1160–1169.
Fraser, R. G., Hickey, N. M., Niklason, L. T., Sabbagh, E. A., Luna, R. F., Alexander, C. B., Robinson, C. A., Katzenstein, A. L. & Barnes, G. T. (1986). *Radiology*, **160**, 595–601.
Goto, S., Takeshita, K., Suzuki, Y., Ohashi, H., Asano, Y., Kimura, H., Matsushita, T., Yagi, N., Isshiki, M., Yamazaki, H., Yoneda, Y., Umetani, K. & Ishikawa, T. (2001). *Nucl. Instrum. Methods Phys. Res. A*, **467–468**, 682–685.
Graser, A., Johnson, T. R., Bader, M., Staehler, M., Haseke, N., Nikolaou, K., Reiser, M. F., Stief, C. G. & Becker, C. R. (2008). *Invest. Radiol.* **43**, 112–119.
Hooper, S. B., Kitchen, M. J., Siew, M. L. L., Lewis, R. A., Fouras, A., te Pas, A. B., Siu, K. K. W., Yagi, N., Uesugi, K. & Wallace, M. J. (2009). *Clin. Exp. Pharmacol. Physiol.* **36**, 117–125.
Ishigaki, T., Sakuma, S., Horikawa, Y., Ikeda, M. & Yamaguchi, H. (1986). *Radiology*, **161**, 271–273.
Jensen, M. D., Kanaley, J. A., Reed, J. E. & Sheedy, P. F. (1995). *Am. J. Clin. Nutr.* **61**, 274–278.
Kelcz, F., Zink, F. E., Peppler, W. W., Kruger, D. G., Ergun, D. L. & Mistretta, C. A. (1994). *Am. J. Roentgenol.* **162**, 271–278.
Kitchen, M. J., Lewis, R. A., Morgan, M. J., Wallace, M. J., Siew, M. L. L., Siu, K. K. W., Habib, A., Fouras, A., Yagi, N., Uesugi, K. & Hooper, S. B. (2008). *Phys. Med. Biol.* **53**, 6065–6077.
Kitchen, M. J., Paganin, D. M., Uesugi, K., Allison, B. J., Lewis, R. A., Hooper, S. B. & Pavlov, K. M. (2011). *Phys. Med. Biol.* **56**, 515–534.
Lehmann, L. A., Alvarez, R. E., Macovski, A., Brody, W. R., Pelc, N. J., Riederer, S. J. & Hall, A. L. (1981). *Med. Phys.* **8**, 659–667.
NIST (2011). *X-ray Mass Attenuation Coefficients*, http://www.nist.gov/pml/data/xraycoef/index.cfm.
Phillips (2008). *Exploring the spectrum – advances and potential of spectral CT*, http://clinical.netforum.healthcare.philips.com/us_en/Explore/White-Papers/CT/Exploring-the-spectrum-Advances-and-potential-of-spectral-CT.
Sartoris, D. J. & Resnick, D. (1989). *Am. J. Roentgenol.* **152**, 241–246.
Schwarz, F., Ruzsics, B., Schoepf, U. J., Bastarrika, G., Chiaramida, S. A., Abro, J. A., Brothers, R. L., Vogt, S., Schmidt, B., Costello, P. & Zwerner, P. L. (2008). *Eur. J. Radiol.* **68**, 423–433.
Snigirev, A., Snigireva, I., Kohn, V., Kuznetsov, S. & Schelokov, I. (1995). *Rev. Sci. Instrum.* **66**, 5486–5492.
Speller, R. D., Ensell, G. J. & Wallis, C. (1983). *Brit. J. Radiol.* **56**, 461–465.
Suzuki, K., Abe, H., MacMahon, H. & Doi, K. (2006). *IEEE Trans. Med. Imaging*, **25**, 406–416.
Thieme, S. F., Becker, C. R., Hacker, M., Nikolaou, K., Reiser, M. F. & Johnson, T. R. (2008). *Eur. J. Radiol.* **68**, 369–374.
Torikoshi, M., Tsunoo, T., Endo, M., Noda, K., Kumada, M., Yamada, S., Soga, F. & Hyodo, K. (2001). *J. Biomed. Opt.* **6**, 371–377.
Torikoshi, M., Tsunoo, T., Sasaki, M., Endo, M., Noda, Y., Ohno, Y., Kohno, T., Hyodo, K., Uesugi, K. & Yagi, N. (2003). *J. Biomed. Opt.* **48**, 673–685.
Uesugi, K., Hoshino, M. & Yagi, N. (2011). *J. Synchrotron Rad.* **18**, 217–223.
Wilkins, S. W., Gureyev, T. E., Gao, D., Pogany, A. & Stevenson, A. W. (1996). *Nature (London)*, **384**, 335–338.
Xu, T., Ducote, J. L., Wong, J. T. & Molloi, S. (2011). *Phys. Med. Biol.* **56**, 1191–1205.